

Polarization Enhancement in Perovskite Superlattices by Oxygen Octahedral Tilts

X. Z. Lu, X. G. Gong and H. J. Xiang*

Key Laboratory of Computational Physical Sciences (Ministry of Education), State

Key Laboratory of Surface Physics, and Department of Physics, Fudan University,

Shanghai 200433, P. R. China

e-mail: hxiang@fudan.edu.cn

Abstract

Interface engineering in perovskite oxide superlattices has developed into a flourishing field, enabling not only further tuning of the exceptional properties, but also giving access to emergent physical phenomena. Here, we reveal a new mechanism for enhancing the electric polarization by the interfacial oxygen octahedral tilts in BaTiO₃/CaTiO₃ superlattices. By combining a novel genetic algorithm with density functional theory (DFT), we predict that the true ground states in 1:1 and 2:2 BaTiO₃/CaTiO₃ superlattices grown on SrTiO₃ adopt the *Pc* symmetry with a large electric polarization (32.7 μC/cm² for 1:1 and 34.0 μC/cm² for 2:2 superlattices), which is even larger than that of bulk BaTiO₃. The tilt of oxygen octahedron is found to play a key role for the enhancement of out-of-plane polarization because it reduces greatly the rotation of oxygen octahedron which significantly suppresses the out-of-plane polarization.

Introduction

Interfaces formed by perovskite oxides offer a tremendous opportunity for fundamental as well as applied research. In this active field of research, interfacial effects on the polarization of the ultra-short superlattices have attracted enormous interests¹⁻⁸. Considering only the out-of-plane ferroelectric modes, Neaton *et al.* predicted that the polarization of BaTiO₃/SrTiO₃ superlattices (*P4mm* structure) with BaTiO₃ (BTO) fraction larger than 40% grown on the SrTiO₃ (STO) substrate was enhanced above that of bulk BTO¹. The effects of oxygen octahedral rotations around [001] on the ferroelectricity were examined later: It was shown that a trilinear coupling between the ferroelectric and interfacial (in-phase and out-of-phase) antiferrodistortive (AFD) rotation modes results in an enhanced polarization in the 1:1 PbTiO₃/SrTiO₃ (PTO/STO) superlattices with octahedral rotations (*P4bm* structure) when compared to the *P4mm* structure^{7,9}. However, the role of another common AFD mode, i.e., oxygen octahedral tilt (rotation of oxygen octahedron around an axis perpendicular to [001]) played on the polarization has never been elucidated.

In this work, we address this issue by investigating a typical ferroelectric/dielectric superlattice system, i.e., (BaTiO₃)_n/(CaTiO₃)_n (*n* is the number of layers). Previous first principles studies showed that the polarization of (BaTiO₃)₂/(CaTiO₃)₂ on the STO substrate with the *P4mm* structure was larger than that of the tetragonal bulk BTO¹⁰. But it decreased greatly in *P4bm* structure and became even smaller than the tetragonal bulk BTO value. This decreasing was attributed to the suppressing of the polarization by an oxygen octahedral rotation^{11,12}.

It should be noted that all previous studies neglected the tilts of oxygen octahedra, which is one of the most important distortions in bulk *Pbnm* CaTiO₃.

In order to consider all possible relevant distortions in perovskites, we propose a global optimization method based on the genetic algorithm (GA) (see Methods) to search the lowest energy structures of the BTO/CTO superlattices. By combining the GA with density functional theory (DFT) calculations, the true ground states of 1:1 and 2:2 BTO/CTO superlattices are predicted to adopt the *Pc* symmetry. We find that the out-of-plane polarization in the *Pc* structure with oxygen octahedral tilts is enhanced. This is because the tilts of oxygen octahedra suppress dramatically the oxygen octahedral rotations, which disfavor the out-of-plane ferroelectricity. Finally due to the existence of a large in-plane polarization, the total polarizations of 1:1 and 2:2 BTO/CTO on STO are predicted to be 32.7 $\mu\text{C}/\text{cm}^2$ and 34.0 $\mu\text{C}/\text{cm}^2$ respectively, which are larger than the bulk value of tetragonal BTO.

Results

The lattice vectors used in this study are $\mathbf{a} = a_s\mathbf{x} - a_s\mathbf{y}$, $\mathbf{b} = a_s\mathbf{x} + a_s\mathbf{y}$ and $\mathbf{c} = \delta_1\mathbf{x} + \delta_2\mathbf{y} + (2a_s + \delta_3)\mathbf{z}$ for 20-atom cell and $\mathbf{c} = \delta_1\mathbf{x} + \delta_2\mathbf{y} + (4a_s + \delta_3)\mathbf{z}$ for 40-atom cell, where a_s is the in-plane lattice constant of the studied system at a given strain, and $(\mathbf{x}, \mathbf{y}, \mathbf{z})$ are defined within the pseudocubic setting. Epitaxial strain is then defined as $(a_s - a_0)/a_0$, where a_0 (3.856 Å) is the theoretical lattice constant of bulk STO within the LDA optimization in ref. 11.

The total energies of the lowest energy phases in 1:1 BTO/CTO superlattices from the GA simulations, as a function of epitaxial strain from -4% to 4% , are

shown in Figure 1a. For comparison, the previous suggested $P4bm$, $P4mm$ and Pm ¹³ phases are also shown. Fig. 1b displays the dependence of the total polarizations of the lowest energy phases on the epitaxial strain for 1:1 superlattices. The results for 2:2 superlattices are given in Supplementary Part 1.

As can be seen in Fig. 1a, in the strain range of -4% - 1%, Pc phase is stabilized, which is lower in energy by about 14 meV per formula unit with respect to $P4bm$ phase. This is also confirmed by the phonon calculations indicating that the $P4bm$ structure is unstable. In the Pc structure, the tilts of oxygen octahedra and the in-plane ferroelectric distortion occur which lower the energy when compared with the $P4bm$ structure. These rotations and tilts of oxygen octahedra related to the CTO bulk-like layers can be attributed to the interfacial effects, which do not exist in the BTO bulk. As the strain is higher than 1%, the Pc phase is gradually transformed into the $Pmc2_1$ phase. The phase diagram for 2:2 superlattices is similar to that of 1:1 superlattices, but the stable region for the Pc phase is -4% - 2% and 2% - 4% for the $Pmc2_1$ phase (see Supplementary Fig. S1). Although these two phases were also found in 1:1 and 2:2 PTO/STO superlattices⁹, the range of the Pc phase is much wider in BTO/CTO, i.e. -4% - 1% for 1:1 superlattices and -4% - 2% for 2:2 superlattices, to be compared with -1% - 1% for 2:2 PTO/STO and a negligible range for 1:1 PTO/STO⁹. This is due to the fact that the instability of the tilt of oxygen octahedron still exists at -4% strain in our case (see Supplementary Table SII). The monoclinic Pc structure has both in-plane and out-of-plane ferroelectric components. As shown in Table I, the out-of-plane polarization in the Pc structure is larger than that in the $P4bm$ structure at

0% strain and will gradually increase with increasing the compressive strain (see Fig. 1b). Combined with the in-plane component, the total polarization for the 1:1 BTO/CTO ($32.7 \mu\text{C}/\text{cm}^2$ when grown on the [001] STO) is even larger than that ($25.4 \mu\text{C}/\text{cm}^2$) of the tetragonal BTO bulk from our theoretical calculation.

Discussion

To find out the origins of this enhancement of out-of-plane polarization in 1:1 BTO/CTO, we carefully investigate the distortions in the Pc structure at 0% strain. The centrosymmetric $P4mmm$ structure is chose to be the reference structure. We find that the Γ^{5-} , Γ^{3-} , M^{5-} , M^{3+} and M^{1-} modes are condensed in this Pc structure, which correspond to in-plane (FE_{xy}) and out-of-plane (FE_z) ferroelectric modes, tilt of oxygen octahedron (AFD_{xy}), in-phase (AFD_{zi}) and out-of-phase (AFD_{zo}) rotations of oxygen octahedra, respectively (see Fig. 2). Phonon calculations show that all these modes are unstable. Interestingly, the magnitude of the phonon frequency for the AFD_{xy} mode (oxygen octahedral tilt) is the largest, indicating that it is more likely to be one of the main structural distortions which drive the phase transition.

We start by investigating the effects of the tilts of oxygen octahedra on the other modes. The relationship between AFD_{zi} and AFD_{xy} modes and that between AFD_{zo} and AFD_{xy} modes are investigated, respectively. We first consider the case where only one mode (either AFD_{zi} or AFD_{zo}) is added to the reference $P4mmm$ structure. Then we also add the same AFD_{xy} tilts as that in the Pc structure. As shown in Fig. 3a, both the magnitudes of AFD_{zi} and AFD_{zo} rotations decrease in the existence of AFD_{xy} tilts. We can also see that the AFD_{zo} rotation related energy change from the $P4bm$

structure to *Pc* structure (from $\theta_Z^I = 0.8^\circ$ and $\theta_Z^O = 6.0^\circ$ to $\theta_Z^I = 2.3^\circ$ and $\theta_Z^O = 3.1^\circ$, where θ_Z^I and θ_Z^O represent the magnitudes of the AFD_{zi} and AFD_{zo} rotations, respectively) is much larger than AFD_{zi} rotation related energy change. The coupling between the AFD_{xy} mode and the modes of the oxygen octahedral rotation can be described phenomenologically by $(\theta_Z^I \theta_{XY})^2$ and $(\theta_Z^O \theta_{XY})^2$ terms (θ_{XY} labels the magnitude of the AFD_{xy} tilt) in the Landau expansion (see Supplementary Part 3). In order to understand the microscopic origin of this coupling between the AFD_{xy} mode and the AFD_{zo} mode, we add the AFD_{xy} and AFD_{zo} modes into the reference structure and consider two cases (see Fig. 3b): (i) $\theta_Z^O = 3.1^\circ$ and $\theta_{XY} = 3.4^\circ$; (ii): $\theta_Z^O = 6.2^\circ$ and the same θ_{XY} as in case (i). Because there exist only rotations and tilts of oxygen octahedra, the lengths of Ti-O bonds will remain almost unchanged. Thus we only examine the differences of the corresponding Ba-O and Ca-O (A-O) bond lengths between these two cases. Because the A-O interaction is mainly ionic, we firstly investigate the effects of the electrostatic interaction in these two cases. The results show that the electrostatic energy is -734.66 eV for case (i) and -733.98 eV for case (ii). Secondly, we also consider the effect of Pauli repulsion when the A-O bond distance becomes shorter than the sum of the ionic radius (2.75 Å for Ba-O bond and 2.4 Å for Ca-O bond¹⁴). As shown in Fig. 3b, we find the shorter Ba-O bond lengths in case (ii) are all less than those in case (i), which indicates that the case (ii) will have stronger repulsion if it exists. Due to the ionic interaction between the A-ion and oxygen atom, the system will decrease the AFD_{zo} rotations in the presence of the AFD_{xy} tilts in order to lower the electrostatic energy and reduce the repulsion. This

mechanism is different from the covalent nature of the different AFD_z rotations in the two interfaces for 2:2 PTO/STO systems in which there exists hybridization between the active lone pair of lead and oxygen atom⁹.

Previously, it was suggested¹¹ that the rotations of oxygen octahedra suppress the out-of-plane polarization (FE_z). Here, we investigate the effects of AFD_{zi} and AFD_{zo} rotations on FE_z in more details. The FE_z polarization as a function of the AFD_{zi} and AFD_{zo} rotations are calculated in which the internal atoms are relaxed according to the FE_z mode with the fixed AFD_{zi} and AFD_{zo} rotations. As can be seen in Fig. 4a, the FE_z polarization decreases greatly with increased AFD_{zo} rotations. As we discussed above, the AFD_{zo} rotations will be suppressed by the AFD_{xy} tilts. As a consequence, the FE_z polarization will increase in the presence of the AFD_{xy} mode (see Fig. 4b). Therefore, AFD_{xy} mode plays an important role in enhancing the FE_z polarization in the Pc structure of 1:1 BTO/CTO. Our proposed mechanism can also be extended to explain the effects of oxygen octahedral tilts on the ferroelectricity in other superlattices. In most cases, the tilts of oxygen octahedra tend to suppress the rotations of oxygen octahedra because the biquadratic coupling terms $(\theta_Z^0 \theta_{XY})^2$ and $(\theta_Z^I \theta_{XY})^2$ are usually positive. If the rotations of the oxygen octahedra suppress the out-of-plane polarization, the FE_z polarization will be enhanced by oxygen octahedral tilts, as the BTO/CTO case we discuss above. If the rotations of the oxygen octahedra enhance the FE_z polarization, then the FE_z polarization will be suppressed by the existence of the tilts of oxygen octahedra. In fact, this is exactly what happened in 1:1 and 2:2 PTO/STO superlattices, where the FE_z polarization of the $P4bm$ structure was

larger than that of the Pc structure⁹.

In summary, a comprehensive study is carried out to investigate the role of the oxygen octahedral tilts played on the polarization of superlattices. We first propose a global optimization method based on the genetic algorithm (GA) to search the ground state structures of superlattices. By using this systematic method, the true ground states for 1:1 and 2:2 BTO/CTO superlattices are predicted to be Pc structures. Then, we find that the FE_z polarization in the Pc structure is larger than that in the $P4bm$ structure, which is due to the fact that the tilts of oxygen octahedra suppress the rotations of oxygen octahedra that disfavor the out-of-plane polarization. More importantly, the new mechanism proposed in this work is generally applicable to other superlattices such as $PbTiO_3/SrTiO_3$. Finally due to the existence of a large in-plane polarization, the total polarizations are predicted to be $32.7 \mu C/cm^2$ for 1:1 and $34.0 \mu C/cm^2$ for 2:2 superlattices when grown on the [001] STO substrate respectively, which are larger than the tetragonal bulk BTO value. Our work suggests that the oxygen octahedral tilt provides a new handle for tuning the exceptional properties in superlattices.

Methods

Since the 1990s, genetic algorithms (GAs) have been used to search the ground state of nanoclusters^{15,16}, alloys^{17,18}, and crystals¹⁹. They employ a search technique based on principles similar to those of natural selection, singling out the most “adaptive” structures, which have the lowest energies^{15,16,19}. In this study, we are dealing with a problem different from the previous studies: Here, the basic lattice

structure (i.e., perovskite based structures) is fixed and our purpose is to find out the distortion of the cell and ionic positions which leads to the lowest energy. To this end, we propose a genetic algorithm which differs from the previous algorithms in several aspects: (1) To generate an initial structure of the first generation, we first randomly select a subgroup of the space group of the undistorted perovskite structure for a given superstructure. By symmetrizing a structure with random distortions using the symmetry operation of the subgroup, we can obtain an initial structure with this selected subgroup symmetry. (2) For the mating operation, we propose another crossover operation besides the usual cut-and-splice method proposed by Deaven and Ho¹⁵: In a cubic perovskite system, there are different unstable phonon modes such as the ferroelectric displacement and the oxygen octahedral rotation. The distortion in the ground state is usually a superposition of different modes. Guided by this physical insight, we introduce the following mating operation:

$$X_{child} = X_{cubic} + (X_{father} - X_{cubic}) + c(X_{mother} - X_{cubic}),$$

where X_{father} and X_{mother} are the two parent structures, X_{cubic} and X_{child} are the undistorted cubic structure and new child structure, respectively. For the new distortion, we take either the sum or difference of these two distortions depending on a constant c , which is randomly chosen to be 1 or -1.

Our total energy calculations are based on the density functional theory (DFT)²⁰ within the local density approximation (LDA) on the basis of the projector augmented wave method²¹ encoded in the Vienna ab initio simulation package²². Calcium 3s, 3p and 4s electrons, Ba 5s, 5p and 6s electrons, Ti 3p, 3d and 4s electrons and O 2s and

2p electrons are treated as valence states. The plane-wave cutoff energy is set to 600 eV for calculating phase diagram and 450 eV for searching the ground state using the GA method. And $4 \times 4 \times 3$ k -point mesh is used for the 20-atom $\sqrt{2} \times \sqrt{2} \times 2$ cell and $4 \times 4 \times 1$ k -point mesh for the 40-atom $\sqrt{2} \times \sqrt{2} \times 4$ cell. For the electric polarization calculations, the berry phase method²³ is used.

References

1. Neaton, J. B. & Rabe, K. M. Theory of polarization enhancement in epitaxial BaTiO₃/SrTiO₃ superlattices. *Appl. Phys. Lett.* **82**, 1586 (2003).
2. Lee, H. N. *et al.* Strong polarization enhancement in asymmetric three-component ferroelectric superlattices. *Nature* **433**, 395-399 (2005).
3. Dawber, M. *et al.* Unusual behavior of the ferroelectric polarization in PbTiO₃/SrTiO₃ superlattices. *Phys. Rev. Lett.* **95**, 177601 (2005).
4. Tian, W. *et al.* Structural evidence for enhanced polarization in a commensurate short-period BaTiO₃/SrTiO₃ superlattice. *Appl. Phys. Lett.* **89**, 092905 (2006).
5. Seo, S. S. A. *et al.* Ferroelectricity in artificial bicolor oxide superlattices. *Adv. Mater.* **19**, 2460- 2464 (2007).
6. Dawber, M. *et al.* Tailoring the properties of artificially layered ferroelectric superlattices. *Adv. Mater.* **19**, 4153- 4159 (2007).
7. Bousquet, E. *et al.* Improper ferroelectricity in perovskite oxide artificial superlattices. *Nature* **452**, 732-736 (2008).
8. Seo, S. S. A. & Lee, H. N. Strain-coupled ferroelectric polarization in BaTiO₃-CaTiO₃ superlattices. *Appl. Phys. Lett.* **94**, 232904 (2009).

9. Aguado-Puente, P., Garcí'a-Ferna ndez, P. & Junquera, J. Interplay of couplings between antiferrodistortive, ferroelectric, and strain degrees of freedom in monodomain $\text{PbTiO}_3/\text{SrTiO}_3$ superlattices. *Phys. Rev. Lett.* **107**, 217601 (2011).
10. Nakhmanson, S. M., Rabe, K. M. & Vanderbilt, D. Polarization enhancement in two- and three-component ferroelectric superlattices. *Appl. Phys. Lett.* **87**, 102906 (2005).
11. Wu, X., Rabe, K. M. & Vanderbilt, D. Interfacial enhancement of ferroelectricity in $\text{CaTiO}_3/\text{BaTiO}_3$ superlattices. *Phys. Rev. B.* **83**, 020104(R) (2011).
12. Swartz, C. W. & Wu, X. Modeling functional piezoelectricity in perovskite superlattices with competing instabilities. *Phys. Rev. B.* **85**, 054102 (2012).
13. Lebedev, A. I. Ground state and properties of ferroelectric superlattices based on crystals of the perovskite family. *Physics of the Solid State* **52**, 1448-1462 (2010).
14. Shannon, R. D. Revised effective ionic radii and systematic studies of interatomic distances in halides and chalcogenides. *Acta Cryst A* **32**, 751-767 (1976).
15. Deaven, D. M. & Ho, K. M. Molecular geometry optimization with a genetic algorithm. *Phys. Rev. Lett.* **75**, 288 (1995).
16. Xiang, H. J., Wei, S.-H. & Gong, X. G. Structures of $[\text{Ag}_7(\text{SR})_4]^-$ and $[\text{Ag}_7(\text{DMSA})_4]^-$. *J. Am. Chem. Soc.* **132**, 7355-7360 (2010).
17. Liu, J. Z., Trimarchi, G. & Zunger, A. Strain-minimizing tetrahedral networks of semiconductor alloys. *Phys. Rev. Lett.* **99**, 145501 (2007).
18. Xiang, H. J., Wei, Su-Huai & Gong, X. G. Structural motifs in oxidized graphene: A genetic algorithm study based on density functional theory. *Phys. Rev. B* **82**,

035416 (2010).

19. Oganov, A. R. & Glass, C. W. Crystal structure prediction using ab initio evolutionary techniques: Principles and applications. *J. Chem. Phys.* **124**, 244704 (2006).
20. Liechtenstein, A. I., Anisimov, V. I. & Zaanen, J. Density-functional theory and strong interactions: Orbital ordering in Mott-Hubbard insulators. *Phys. Rev. B* **52**, R5467-5470 (1995).
21. Blöchl, P. E. Projector augmented-wave method. *Phys. Rev. B* **50**, 17953-17979 (1994); Kresse, G. & Joubert, D. From ultrasoft pseudopotentials to the projector augmented-wave method. *Phys. Rev. B* **59**, 1758-1775 (1999).
22. Kresse, G. & Furthmüller, J. Efficiency of ab-initio total energy calculations for metals and semiconductors using a plane-wave basis set. *Comput. Mater. Sci.* **6**, 15-50 (1996); Efficient iterative schemes for *ab initio* total-energy calculations using a plane-wave basis set. *Phys. Rev. B* **54**, 11169-11186 (1996).
23. King-Smith, R. D. & Vanderbilt, D. Theory of polarization of crystalline solids. *Phys. Rev. B* **47**, 1651-1654 (1993); Resta, R. Macroscopic polarization in crystalline dielectrics: the geometric phase approach. *Rev. Mod. Phys.* **66**, 899-915 (1994).

Acknowledgements

We acknowledge Prof. Xifan Wu and Mr. Hongwei Wang for useful discussions.

Work at Fudan was partially supported by NSFC, the Special Funds for Major State Basic Research, Foundation for the Author of National Excellent Doctoral

Dissertation of China, The Program for Professor of Special Appointment at Shanghai Institutions of Higher Learning, Research Program of Shanghai municipality and MOE.

Author contributions

H.X. and X.L. designed the project and X.L. done the calculations. X.L. and H.X. wrote the manuscript and X.L. prepared the figures. All authors reviewed the manuscript.

Additional information

The authors declare no competing financial interests. Supplementary Information accompanies this paper at <http://www.nature.com/naturecommunications>. Reprints and permissions information is available online at www.nature.com/reprints. Correspondence and requests for materials should be addressed to H.X.

Table I. Calculated polarizations (in $\mu\text{C}/\text{cm}^2$) of the FE modes and magnitudes (in degree) of the AFD modes for 1:1 *Pc* and *P4bm* BTO/CTO superlattice on the [001] STO substrate.

Modes	FE_{xy}	FE_z	AFD_{xy}	AFD_{zi}	AFD_{zo}
<i>Pc</i>	15.7	24.0	3.4	2.3	3.1
<i>P4bm</i>	0.0	19.6	0.0	0.8	6.0

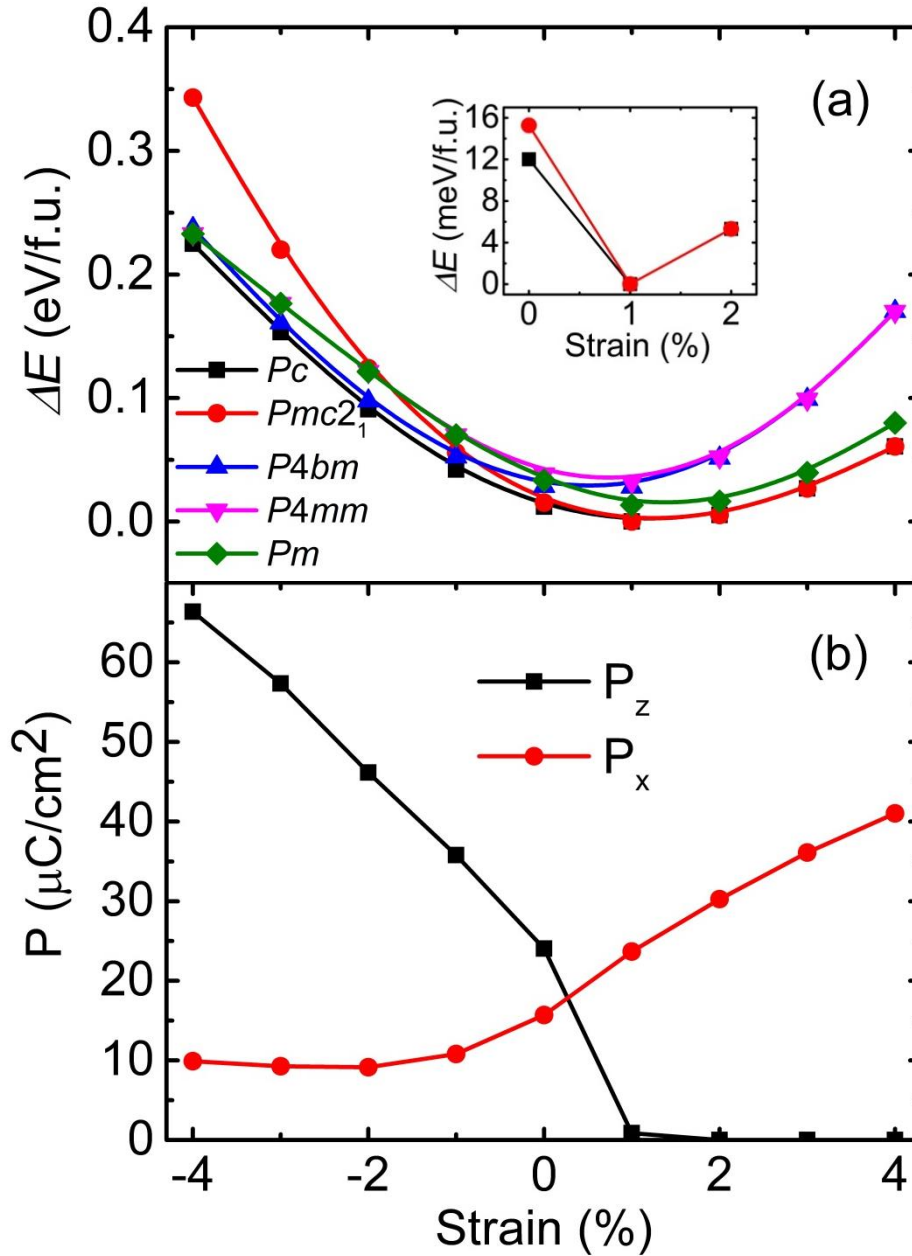


Figure 1. Total energies and electric polarizations of the 1:1 BTO/CTO superlattices. **a**, Calculated total energies versus the epitaxial strain (-4% to 4%) for 1:1 BTO/CTO superlattices. Previously suggested $P4bm$, $P4mm$ and Pm phases are also shown for comparison. Inset shows a zoomed view in the strain range of 0-2%. **b**, Calculated ferroelectric polarizations ($P_y = P_x$) of the lowest energy phases at each strain.

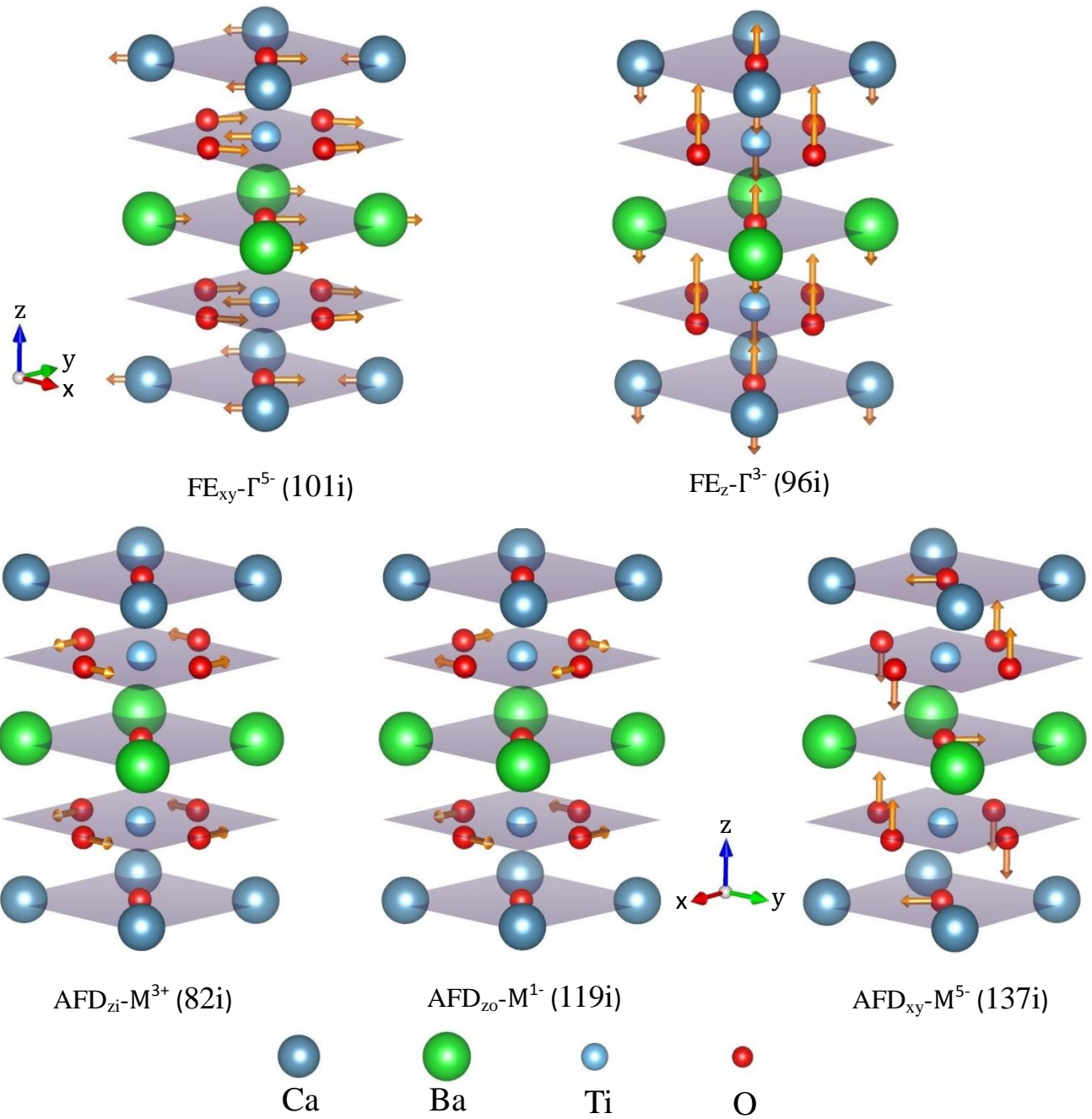


Figure 2. Schematic view of the atomic displacements of unstable modes at Γ and M in the $P4mmm$ structure of a 1:1 BTO/CTO superlattice on the [001] STO substrate.

The numbers in the brackets indicate the phonon frequencies (in cm^{-1}).

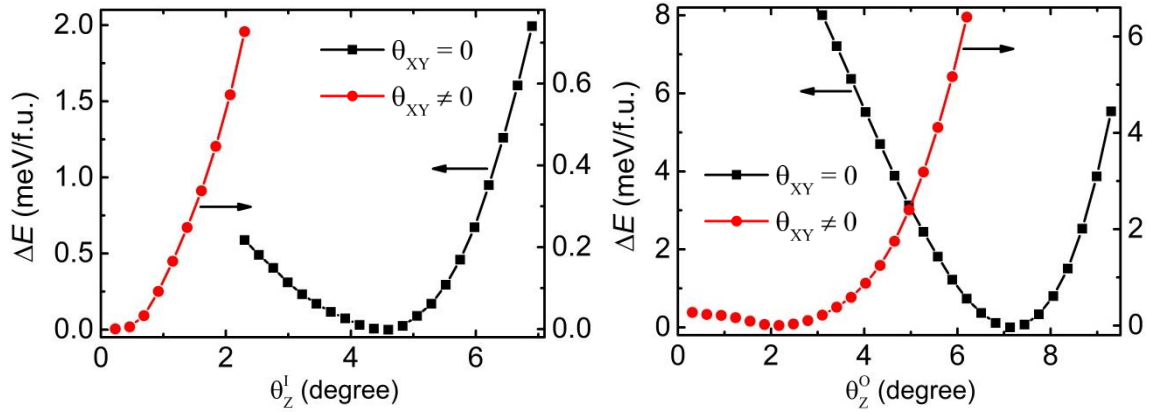
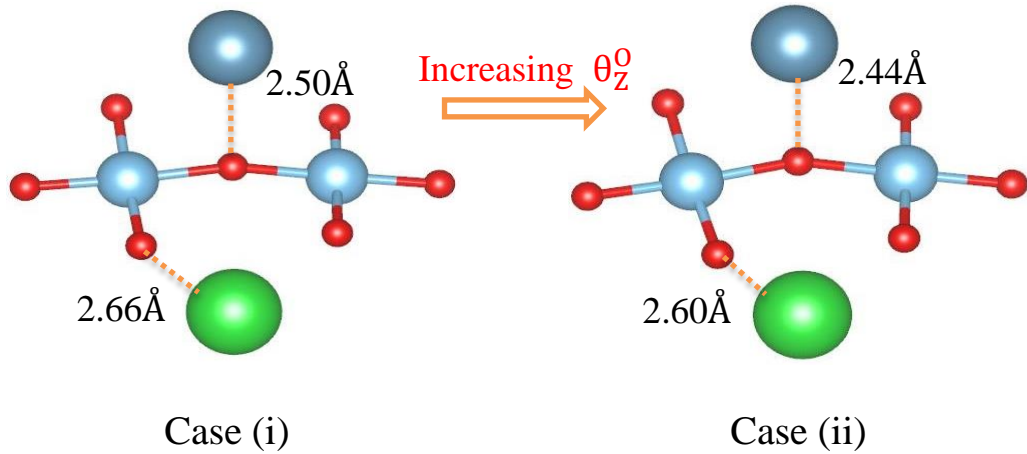
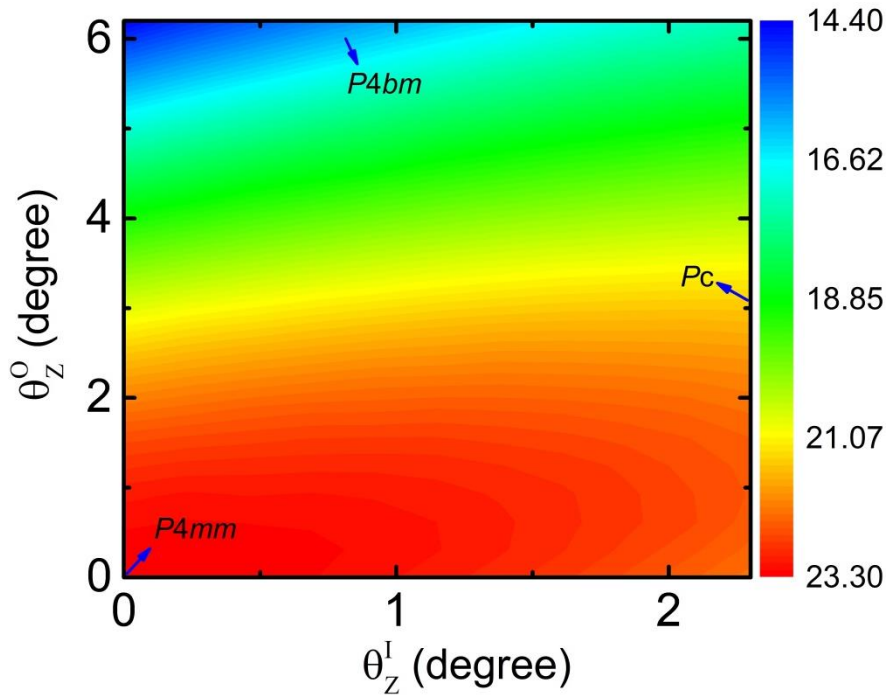
a**b**

Figure 3. Couplings between oxygen octahedral rotations and oxygen octahedral tilts.

a, Energy as a function of the rotation of oxygen octahedron with (right axis) and without (left axis) AFD_{XY} tilts. Left and right panels show the in-phase rotation and out-of-phase rotation, respectively. **b**, Bond lengths of Ba-O and Ca-O bonds comparison between the two cases (i): $\theta_z^0 = 3.1^\circ$ and $\theta_{XY} = 3.4^\circ$; (ii): $\theta_z^0 = 6.2^\circ$ with θ_{XY} as in case (i), where θ_z^0 and θ_{XY} represent the magnitudes of out-of-phase rotation and tilt of oxygen octahedra, respectively. Only Ba-O bonds distances shorter than the summation of the two bonded ions' ionic radius (2.75 Å for

Ba-O bond and 2.4 Å for Ca-O bond) and the shortest Ca-O bonds in changing are shown.

a



b

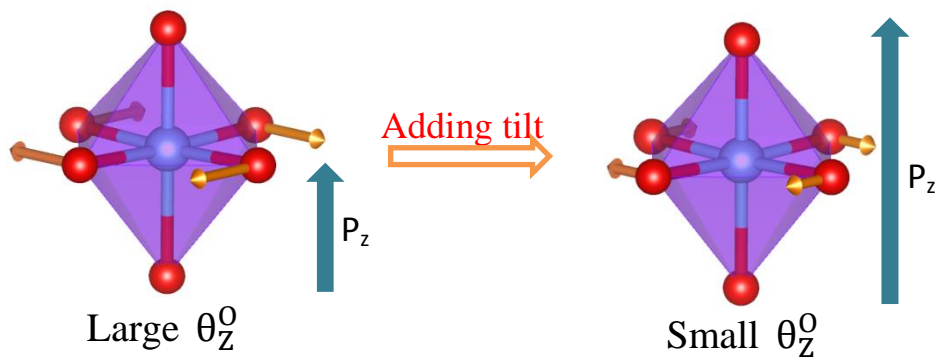


Figure 4. Coupling between the out-of-plane polarization and oxygen octahedral rotations, and new mechanism for enhancing polarization by oxygen octahedral tilts. **a**, Contour plot of the FE_z polarization as a function of θ_z^I and θ_z^0 , where θ_z^I and θ_z^0 are defined as those in the text. The FE_z polarization (in $\mu\text{C}/\text{cm}^2$) gradually increases

from blue color ($14.40 \mu\text{C}/\text{cm}^2$) to red color ($23.30 \mu\text{C}/\text{cm}^2$). Pc , $P4bm$ and $P4mm$ indicate the magnitudes of AFD_{zi} and AFD_{zo} rotations in each case, respectively. **b**, Schematic illustrations of the mechanism of enhancing the FE_z polarization through suppressing the AFD_{zo} rotations by the AFD_{xy} tilts. The yellow arrows indicate the displacements of the oxygen atoms and the blue ones indicate the FE_z polarizations.

Supplementary Materials for
**Polarization Enhancement in Perovskite Superlattices by Oxygen
Octahedral Tilts**

X. Z. Lu, X. G. Gong and H. J. Xiang*

Key Laboratory of Computational Physical Sciences (Ministry of Education), State

Key Laboratory of Surface Physics, and Department of Physics, Fudan University,

Shanghai 200433, P. R. China

1. Phase diagram and physical properties for 2:2 BaTiO₃/CaTiO₃ superlattices.

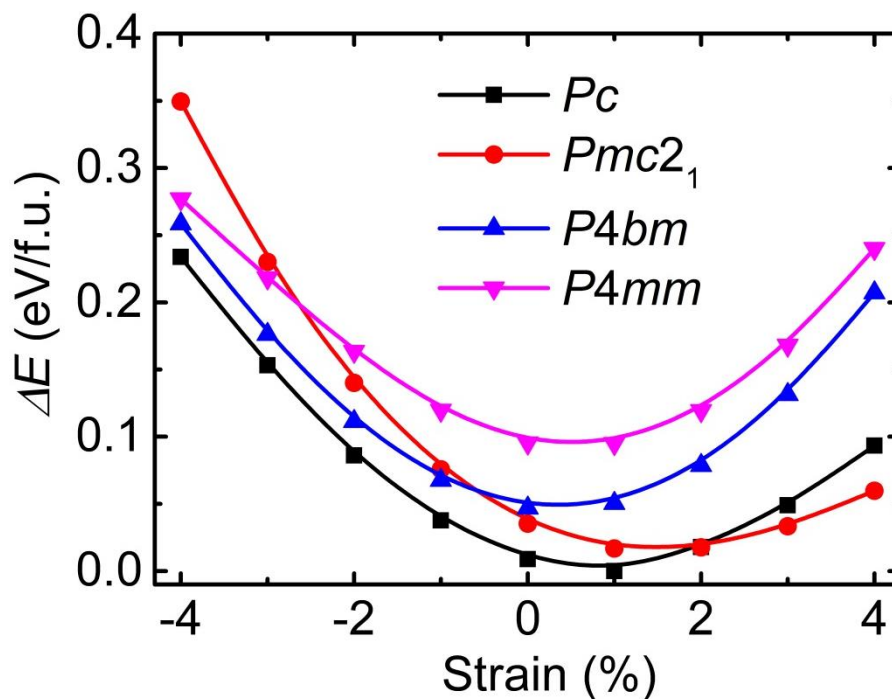


Figure S1. Calculated total energies versus the epitaxial strains in the range of -4-4% for 2:2 BaTiO₃/CaTiO₃ superlattices. Only energy-lowest phases are shown except for the *P4bm* and *P4mm* phases for comparison.

In this 2:2 superlattices, the same space groups as those in 1:1 superlattices for the ground states can be found, i.e., *Pc* phase in the strain range of -4-2% and *Pmc2*₁ phase with the strain higher than 2%. The *Pc* phase is lower in energy by average 36 meV per formula unit with respect to the *P4bm* phase.

Table SI. Calculated FE polarizations (in $\mu\text{C}/\text{cm}^2$) for 2:2 Pc and $P4bm$ BTO/CTO superlattices on the [001] STO substrate.

Modes	FE_{xy}	FE_z
Pc	14.4	27.2
$P4bm$	0.0	19.1

From the above Table, we can find that the FE_z polarization in the 2:2 Pc superlattice is much larger than that in the $P4bm$ superlattice and even slightly larger than that in the 1:1 Pc superlattice. This enhancement of the polarization in the 2:2 Pc superlattice can be attributed to the suppression of the oxygen octahedral rotations by the oxygen octahedral tilts as the case of the 1:1 Pc superlattice discussed in the main text.

2. Phonon calculation for 1:1 BaTiO₃/CaTiO₃ superlattice at -4% strain.

Table SII. Calculated phonon frequencies of unstable modes at Γ and M in the $P4mmm$ structure of a 1:1 BTO/CTO superlattice at -4% strain.

Modes	FE _{xy}	FE _z	AFD _{xy}	AFD _{zi}	AFD _{zo}
ω (cm ⁻¹)	0.3i	259i	162i	192i	207i

3. Couplings between AFD_{zi} and AFD_{xy} modes and between AFD_{zo} and AFD_{xy} modes

Table SIII. Values (in meV) of the coefficients in the model described below.

α^i	β^i	γ^i	α^{ii}	β^{ii}	γ^{ii}
-0.57	1.43×10^{-2}	0.10	-1.87	1.84×10^{-2}	0.14

The free energy can be expanded in terms of the order parameters of FE_{xy} , FE_z , AFD_{xy} , AFD_{zi} and AFD_{zo} modes. To describe the couplings between AFD_{zi} (θ_Z^I) and AFD_{xy} (θ_{XY}) modes and between AFD_{zo} (θ_Z^O) and AFD_{xy} modes, we only need to consider the following terms:

(i) coupling between AFD_{zi} and AFD_{xy} modes:

$$E^i = \alpha^i(\theta_Z^I)^2 + \beta^i(\theta_Z^I)^4 + \gamma^i(\theta_Z^I\theta_{XY})^2 + \text{the others}$$

(ii) coupling between AFD_{zo} and AFD_{xy} modes:

$$E^{ii} = \alpha^{ii}(\theta_Z^O)^2 + \beta^{ii}(\theta_Z^O)^4 + \gamma^{ii}(\theta_Z^O\theta_{XY})^2 + \text{the others}$$

where α^i , β^i , γ^i , α^{ii} , β^{ii} and γ^{ii} are coefficients (the angles θ_Z^I , θ_Z^O , and θ_{XY} are in degree). After the numerical DFT calculations, the values of the coefficients are obtained, as listed in Table SIII. For the coupling between AFD_{zi} and AFD_{xy} modes, if $\theta_{XY}=3.4^\circ$, $\alpha^i + \gamma^i\theta_{XY}^2 > 0$, indicating that the AFD_{zi} rotation is completely suppressed by the AFD_{xy} tilt when $\theta_{XY}=3.4^\circ$, in excellent agreement with the direct DFT result (see left panel of Fig. 3a of the text). For the coupling between AFD_{zo} and AFD_{xy} modes, $\alpha^{ii} + \gamma^{ii}\theta_{XY}^2 < 0$ when $\theta_{XY}=3.4^\circ$, which indicates that the AFD_{zo} rotation will be not completely suppressed by the AFD_{xy} tilt but with a value of 2.4° when $\theta_{XY}=3.4^\circ$, consistent with the direct DFT calculations (see right panel of Fig. 3a

of the text).